Kinetics of Electron Transfer Reactions of H₂-Evolving Cobalt Diglyoxime Catalysts

Jillian L. Dempsey, Jay R. Winkler,* and Harry B. Gray*

Beckman Institute, California Institute of Technology, Pasadena, California 91125

Received September 21, 2009; E-mail: winklerj@caltech.edu; hbgray@caltech.edu

Abstract: Co−diglyoxime complexes catalyze H₂ evolution from protic solutions at modest overpotentials. Upon reduction to Co^I, a Co^{III}-hydride is formed by reaction with a proton donor. Two pathways for H₂ production are analyzed: one is a heterolytic route involving protonation of the hydride to release H₂ and generate Co^{III}; the other is a homoytic pathway requiring association of two Co^{III}-hydrides. Rate constants and reorganization parameters were estimated from analyses of laser flash−quench kinetics experiments (Co^{III}−Co^{II} self-exchange $k = 9.5 \times 10^{-8} - 2.6 \times 10^{-5}$ M^{-1} s^{-1}; $\lambda = 3.9$ (± 0.3) eV: Co^{II}−Co^I self-exchange $k = 1.2$ (± 0.5) $\times 10^5$ M^{-1} s^{-1}; $\lambda = 1.4$ (± 0.05) eV). Examination of both the barriers and driving forces associated with the two pathways indicates that the homolytic reaction ($Co^{III}H + Co^{III}H \rightarrow 2 Co^{II} + H_2$) is favored over the route that goes through a Co^{III} intermediate ($Co^{III}H + H^+ \rightarrow Co^{III} + H_2$).

1. Introduction

Energy-efficient solar water splitting requires a catalyst that can use photochemically generated reducing equivalents to produce molecular hydrogen from protic solutions with high turnover frequency.[1,2] Practical solar hydrogen production depends on minimizing the release of free energy, yet most molecular H₂-evolution catalysts operate with substantial overpotentials (−0.9 to −1.8 V vs SHE).[3] We are investigating the kinetics and thermodynamics of active Co^{II} catalysts in order to elucidate the barriers associated with elementary steps involved in H₂ evolution.

A Co^{III}-hydride ($Co^{III}H$) formed in the reaction between a Co^I complex and a proton donor (HA) likely is a key intermediate in the catalytic cycle.[4] Production of H₂ from $Co^{III}H$ can occur via homolysis (Figure 1, red path) or heterolysis (Figure 1, blue path) of the Co^{III}−H bond.[5,6] Efficient catalysis by the heterolytic pathway demands that the Co^{III} product of Co^{III}−H bond heterolysis be converted rapidly to Co^{II} in the pool of reducing equivalents.

Difluoroboryl-bridged Co^{II}−diglyoxime complexes ([Co-(dpgBF₂)₂(CH₃CN)₂], [Co(dmgBF₂)₂(CH₃CN)₂]: dpg = difluoroboryl-diphenylglyoxime, dmg = difluoroboryl-dimethylglyoxime)[7] are among a handful of catalysts[8] that operate at relatively high rates with modest overpotentials. We have
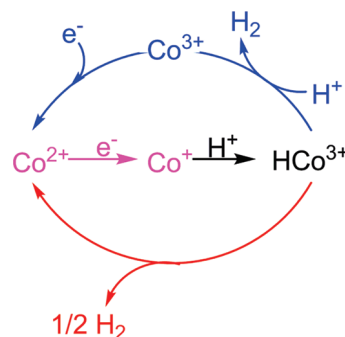

Figure 1. Homolytic (red) and heterolytic (blue) reaction pathways for catalysis of H₂ evolution by Co^{II} complexes. Reducing equivalents (D) deliver electrons to Co^{II} complexes, and the resulting Co^I species are protonated to form $Co^{III}H$ intermediates. In the homolytic pathway, two $Co^{III}H$ species undergo bimolecular reductive elimination to produce H₂. In the heterolytic pathway, protonation of $Co^{III}H$ is responsible for H₂ release, and the Co^{III} species is reduced back to Co^{II} by D.

employed a laser flash−quench method[9,10] to trigger the reduction of **Co^{II}** ([Co(dpgBF₂)₂(CH₃CN)₂]) to **Co^I** ([Co-(dpgBF₂)₂(CH₃CN)]⁻), and time-resolved spectroscopy to identify and monitor the short-lived species. This method permits observation of discrete intermediates on time scales appreciably shorter than those accessible by conventional stopped-flow spectroscopy. Analyses of these flash−quench kinetics data have revealed the barriers for key elementary steps in the catalytic cycle leading to the formation of H₂.

(1) Esswein, A. J.; Nocera, D. G. *Chem. Rev.* **2007**, *107*, 4022–4047.
(2) (a) Du, P.; Schneider, J.; Luo, G.; Brennessel, W. W.; Eisenberg, R. *Inorg. Chem.* **2009**, *48*, 4952–4962. (b) Lazarides, T.; McCormick, T.; Du, P.; Luo, G.; Lindley, B.; Eisenberg, R. *J. Am. Chem. Soc.* **2009**, *131*, 9192–9194. (c) Fihri, A.; Artero, V.; Pereira, A.; Fontecave, M. *Dalton Trans.* **2008**, 5567–5569. (d) Probst, B.; Kolano, C.; Hamm, P.; Alberto, R. *Inorg. Chem.* **2009**, *48*, 1836–1843.
(3) General reviews on transition metal hydrogen evolution catalysts: (a) Artero, V.; Fontecave, M. *Coord. Chem. Rev.* **2005**, *249*, 1518–1535. (b) Koelle, U. *New. J. Chem.* **1992**, *16*, 157–169.
(4) Connolly, P.; Espenson, J. H. *Inorg. Chem.* **1986**, *25*, 2684–2688.
(5) Baffert, C.; Artero, V.; Fontecave, M. *Inorg. Chem.* **2007**, *46*, 1817–1824.
(6) Hu, X.; Brunschwig, B. S.; Peters, J. C. *J. Am. Chem. Soc.* **2007**, *129*, 8988–8998.

(7) Hu, X.; Cossairt, B. M.; Brunschwig, B. S.; Lewis, N. S.; Peters, J. C. *Chem. Commun.* **2005**, 4723–4725.
(8) (a) Appel, A. M.; DuBois, D. L.; DuBois, M. R. *J. Am. Chem. Soc.* **2005**, *127*, 12717–12726. (b) Wilson, A. D.; Newell, R. H.; McNevin, M. J.; Muckerman, J. T.; DuBois, M. R.; DuBois, D. L. *J. Am. Chem. Soc.* **2006**, *128*, 358–366. (c) Razavet, M.; Artero, V.; Fontecave, M. *Inorg. Chem.* **2005**, *44*, 4786–4795.
(9) Ogata, T.; Yanagida, S.; Brunschwig, B. S.; Fujita, E. *J. Am. Chem. Soc.* **1995**, *117*, 6708–6716.
(10) Bjerrum, M. J.; Casimiro, D. R.; Chang, I.-J.; Di Bilio, A. J.; Gray, H. B.; Hill, M. G.; Langen, R.; Mines, G. A.; Skov, L. K.; Winkler, J. R.; Wuttke, D. S. *J. Bioenerg. Biomembr.* **1995**, *27*, 295–302.
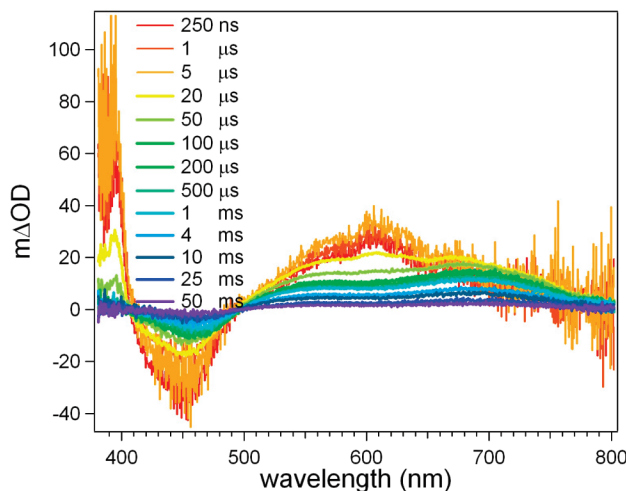
Figure 2. Transient difference spectra 20 μM [Ru(bpy)$_3$][PF$_6$]$_2$, 3.5 mM [MV][PF$_6$]$_2$, 0.1 M NBu$_4$PF$_6$, and 100 μM **Co^{II}** in CH$_3$CN at selected time delays after laser excitation. λ_{ex} = 355 nm.

2. Results

2.1. Photochemistry. The photochemical method utilizes methyl viologen (MV^{2+}) to quench pulsed-laser excited [Ru-(bpy)$_3$]$^{2+}$ (bpy = 2,2′-bipyridine). The reduced viologen species, MV$^{•+}$, delivers an electron to **Co^{II}**, producing anionic **Co^{I}** and [Ru(bpy)$_3$]$^{3+}$ The transient absorption (TA) spectrum recorded 250 ns after excitation is dominated by spectral features characteristic of both [Ru(bpy)$_3$]$^{3+}$, bleaching at 450 nm, and MV$^{•+}$, absorbing at 390 and 605 nm (Figure 2). Between 20 and 100 μs, the shift in the red absorption feature to 686 nm with concomitant loss of the 390 nm absorbance matches the spectroscopic signature of **Co^{I}** (see Figure S1, Supporting Information). During the time interval 500 μs to 50 ms, **Co^{I}** reacts with two oxidants in solution, [Ru(bpy)$_3$]$^{3+}$ and **Co^{III}** ([Co(dpgBF$_2$)$_2$(CH$_3$CN)$_2$]$^+$), the latter produced transiently via [Ru(bpy)$_3$]$^{3+}$ oxidation of **Co^{II}**.

The transient difference spectra were fit with linear combinations of the following three molar difference spectra:
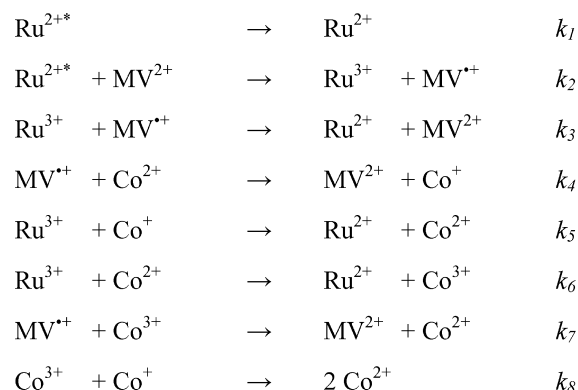
$$\Delta\varepsilon_1(\lambda) = [\varepsilon_{Ru^{3+}}(\lambda) + \varepsilon_{MV^{•+}}(\lambda) - \varepsilon_{Ru^{2+}}(\lambda) - \varepsilon_{MV^{2+}}(\lambda)]$$

$$\Delta\varepsilon_2(\lambda) = [\varepsilon_{Ru^{3+}}(\lambda) + \varepsilon_{Co^+}(\lambda) - \varepsilon_{Ru^{2+}}(\lambda) - \varepsilon_{Co^{2+}}(\lambda)]$$

$$\Delta\varepsilon_3(\lambda) = [\varepsilon_{Co^{3+}}(\lambda) + \varepsilon_{Co^+}(\lambda) - 2\varepsilon_{Co^{2+}}(\lambda)]$$

where $\Delta\varepsilon_1(\lambda)$, $\Delta\varepsilon_2(\lambda)$, and $\Delta\varepsilon_3(\lambda)$ describe differences in molar extinction coefficients between charge transfer pairs. Vectors ($\Delta\mathbf{A}$) describing the time-resolved difference spectra at discrete wavelengths (λ, 400−800 nm) were generated for several delay times, t. A matrix, $\Delta\boldsymbol{\varepsilon}$, was formulated to describe the molar difference spectra described above, $\Delta\boldsymbol{\varepsilon} = [\Delta\varepsilon_1(\lambda), \Delta\varepsilon_2(\lambda), \Delta\varepsilon_3(\lambda)]$. An approximation for $\varepsilon_{Co^{3+}}(\lambda)$ was made ($\varepsilon_{Co^{3+}}(\lambda = 400-800$ nm) = 0), as **Co^{III}** is not isolable. Note, however, that the absorption profile of the **Co^{III}Me** species, Me−Co(dpgBF$_2$)$_2$L, only has a weak feature at 406 nm and a tail into the visible region. As the transient difference spectra should be a linear combination of $\Delta\varepsilon_i$ (i = 1,2,3), the expression $\Delta\mathbf{A} = \Delta\boldsymbol{\varepsilon} \times \boldsymbol{\alpha}$ was solved for $\boldsymbol{\alpha}$ ($\boldsymbol{\alpha} = \Delta\boldsymbol{\varepsilon}^{-1} \times \Delta\mathbf{A}$), where $\boldsymbol{\alpha}$ is a column vector reflecting the contributions of the three molar difference spectra to the experimental spectrum. Fits of the transient spectra were generated using the expression $\Delta\mathbf{A}_{fit} = \Delta\boldsymbol{\varepsilon} \times \boldsymbol{\alpha}$. The process was repeated for time delays of 20, 50, and

Ru^{2+*}		$\rightarrow$	Ru^{2+}		k_1
Ru^{2+*}	+ MV^{2+}	$\rightarrow$	Ru^{3+}	+ MV$^{•+}$	k_2
Ru^{3+}	+ MV$^{•+}$	$\rightarrow$	Ru^{2+}	+ MV^{2+}	k_3
MV$^{•+}$	+ Co^{2+}	$\rightarrow$	MV^{2+}	+ Co$^+$	k_4
Ru^{3+}	+ Co$^+$	$\rightarrow$	Ru^{2+}	+ Co^{2+}	k_5
Ru^{3+}	+ Co^{2+}	$\rightarrow$	Ru^{2+}	+ Co^{3+}	k_6
MV$^{•+}$	+ Co^{3+}	$\rightarrow$	MV^{2+}	+ Co^{2+}	k_7
Co^{3+}	+ Co$^+$	$\rightarrow$	2 Co^{2+}		k_8

100, 200, and 500 μs, and fits were overlaid with the difference spectra (Figure S2, Supporting Information). Small deviations in the fits were observed in the 400−500 nm region and attributed to the approximation made for $\varepsilon_{Co^{3+}}(\lambda)$.

A kinetics model (Scheme 1) was used to describe the photochemical electron transfer (ET) reaction scheme. The decay of the excited state of [Ru(bpy)$_3$]$^{2+}$ is described by rate constant k_1, and measured via time-resolved luminescence. Bimolecular oxidative quenching by MV^{2+} is described by k_2, and the charge recombination by k_3. Stern−Volmer quenching was used to determine k_2; the value was consistent with previous reports.[11] The single-wavelength transient absorption (λ_{ex} = 480 nm, λ_{obs} = 730 nm) of a sample containing 20 μM [Ru(bpy)$_3$][PF$_6$]$_2$, 0.1 M NBu$_4$PF$_6$, 3.5 mM [MV][PF$_6$]$_2$, was modeled with second-order kinetics to obtain a value for k_3 that was consistent with literature reports.[12]

Electron transfer from MV$^{•+}$ to **Co^{II}** is described by k_4. [Ru(bpy)$_3$]$^{3+}$ oxidations of **Co^{I}** and **Co^{II}** are identified with rate constants k_5 and k_6, respectively. Charge recombination reactions between **Co^{III}** and either MV$^{•+}$ or **Co^{I}** are described by k_7 and k_8, respectively. Kinetics simulations were performed with differential equations (Scheme S1, Supporting Information) describing the concentrations of all species involved in these ET reactions. Inputs to solve the initial value problem included a vector describing initial concentrations of reactants and products, a time-span vector (10^{-6} to 10^{-1} s), and a vector of rate constants k_1−k_8. Profiles of concentration changes versus time were plotted for each individual species. These concentration profiles were translated to simulated transient difference spectra by summing the products of a concentration profile multiplied by an estimated absorption coefficient at 730 nm for each species (Table S1, Supporting Information). The rate constants (k_4, k_5, k_6, k_7, and k_8) were iteratively adjusted until a satisfactory simulation of the TA kinetics was obtained (Figure 3). Simulations were repeated for six different sample measurements containing variable amounts of **Co^{II}** (63−157 μM) and were iterated to obtain a self-consistent set of rate constants.

2.2. Rate Constants and Reorganization Energies. The rate constants for electron-exchange reactions of **Co^{III}** and **Co^{II}** as well as **Co^{II}** and **Co^{I}** can be estimated using the Marcus cross relation,[13] $k_{12} = (k_{11}k_{22}K_{12}f_{12})^{1/2}$, where k_{12} describes the rate constant of an ET cross reaction, k_{11} and k_{22} are the self-

(11) Chiorboli, C.; Indelli, M. T.; Scandola, M. A. R.; Scandola, F. *J. Phys. Chem.* **1988**, *92*, 156–163.
(12) Clark, C. D.; Hoffman, M. Z. *J. Phys. Chem.* **1996**, *100*, 7526–7532.
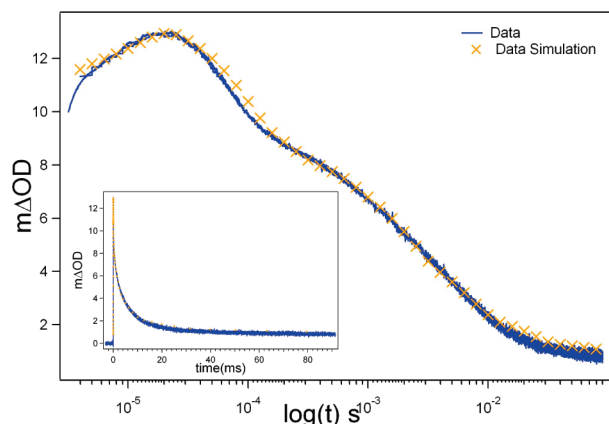(13) Marcus, R. A.; Sutin, N. *Biochem. Biophys. Acta* **1985**, *811*, 265–322.

Figure 3. Kinetics trace of 20 μM [Ru(bpy)$_3$][PF$_6$]$_2$, 3.5 mM [MV][PF$_6$]$_2$, 0.1 M NBu$_4$PF$_6$, 125 μM **Co^{II}**, and the simulated fit in logarithmic time. λ_{ex} = 480 nm, λ_{obs} = 730 nm. ET rate constants used in the simulation: k_1, 1.04 × 10^6 s^{-1}; k_2, 1.58 × 10^9 M^{-1} s^{-1}; k_3, 5.7 × 10^9 M^{-1} s^{-1}; k_4, 2.0 × 10^8 M^{-1} s^{-1}; k_5, 9.8 × 10^9 M^{-1} s^{-1}; k_6, 5.2 × 10^7 M^{-1} s^{-1}; k_7, 6.0 × 10^6 M^{-1} s^{-1}; k_8, 4.4 × 10^8 M^{-1} s^{-1}. Inset: kinetics and fit plotted on a linear time axis.

exchange reaction rate constants, K_{12} is the equilibrium constant for the cross reaction, f_{12} is a known function of these parameters, $\ln f_{12} = ((\ln K_{12})^2)/(4 \ln ((k_{11}k_{22})/Z^2))$, and Z is the collision frequency, estimated to be 10^{11} M^{-1} s^{-1}.

To solve for the self-exchange rate constants of the cobalt redox pairs, the specific rate for [Ru(bpy)$_3$]$^{3+/2+}$ self-exchange was taken from literature data. There are two generally accepted values for this rate constant; 2.0 × 10^9 M^{-1} s^{-1} at 25 °C in 1 M HClO$_4$(aq) reported by Meyer and co-workers[14] and 8.3 × 10^6 M^{-1} s^{-1} at 25 °C in CH$_3$CN obtained by Chan and Wahl.[15] Temperature dependence measurements allow us to extrapolate the latter value to 7.3 × 10^6 M^{-1} s^{-1} at 20 °C. Using these rate constants as limiting values, we estimated ranges for the self-exchange rate constants for **Co^{III}**−**Co^{II}** and **Co^{II}**−**Co^{I}**.

The cross reaction of [Ru(bpy)$_3$]$^{3+}$ + MV$^{•+}$ → [Ru(bpy)$_3$]$^{2+}$ + MV^{2+} (k_3) gave self-exchange rate constants for MV$^{2+/•+}$ (6.2 × 10^2 and 1.7 × 10^5 M^{-1} s^{-1}) that were 3−6 orders of magnitude smaller than the literature value (5.4 × 10^8 M^{-1} s^{-1}).[16] The deviation can be attributed to the fact that the Marcus cross relation does not take into account inverted driving force effects or diffusion limits. For later calculations, k_{11} for MV$^{2+/•+}$ was assigned the literature value.[16] The self-exchange rate constants calculated for **Co^{III}**−**Co^{II}** and **Co^{II}**−**Co^{I}** are set out in Table 1. The reorganization parameter, λ, is estimated from self-exchange rate constants via $k_{11} = Z\, e^{((-\lambda_{11})/(4RT))}$, where R is the molar gas constant, and T is temperature.

2.3. Thermodynamic Analysis. The driving forces ($-\Delta G^\circ$) for the elementary steps associated with H$_2$ evolution were calculated as described in Figure 4 and Table S3, Supporting Information. The driving force for proton reduction ($-\Delta G_R^\circ$) is the difference between the standard potential for hydrogen evolution by proton donor HA[17] (E°(HA/H$_2$)) and the reduction potential of the reducing equivalent, D.

The driving force for reduction of **Co^{II}** by reductant D is described by $-\Delta G_1^\circ$ and $-(\Delta G_2^\circ - \Delta G_1^\circ)$. The driving force for protonation of **Co^{I}** ($-(\Delta G_{2a}^\circ - \Delta G_1^\circ)$, $-(\Delta G_3^\circ - \Delta G_2^\circ)$, and $-(\Delta G_4^\circ - \Delta G_3^\circ)$) is proportional to the pK_a difference between

HA and Co^{III}H. With sufficiently powerful reductants and proton sources, these steps are exergonic.

In the homolytic reaction pathway, the driving force for the elementary step for H$_2$ evolution is $-\Delta G_{H_2}^\circ$, the difference between ΔG_R° and ΔG_4°. The driving force for the elementary H$_2$ formation step in the heterolytic proton reduction pathway ($\Delta G_{H_{2a}}^\circ$) depends on the average of E°(**Co$^{III/II}$**) and E°(**Co$^{II/I}$**), relative to the proton reduction potential, and the pK_a difference of HA and Co^{III}H. To estimate a lower limit for $\Delta G_{H_{2a}}^\circ$, we assume pK_a(HA) = pK_a(Co^{III}H); thus, $\Delta G_{H_{2a}}^\circ > F[E^\circ_{Co^{II}/Co^I} + E^\circ_{Co^{III}/Co^{II}} - 2E^\circ_{HA/H_2}]$.

The barriers for electron transfer from D to **Co^{II}** ($\Delta G_{ET1}^\ddagger$ and D to **Co^{III}** ($\Delta G_{ET2}^\ddagger$) depend both on the driving forces and reorganization parameters. We assume E°(D$^{+/0}$) = E°(**Co$^{II/I}$**) and a range of self-exchange reorganization energies for the D$^{+/0}$ couple ($\lambda_{11} = 0-1.5$ eV). We take λ_{22}(**Co$^{II/I}$**) = 1.4 eV and λ_{22}(**Co$^{III/II}$**) = 3.9 eV, as calculated above, and the reorganization energy for the cross reactions as $\lambda_{12} = 1/2(\lambda_{11} + \lambda_{22})$. The activation free-energy change for reduction of **Co^{II}** is $\Delta G^\ddagger$(**Co$^{II/I}$**) = λ_{12}(**Co$^{II/I}$**)/4 (4−8 kcal mol^{-1}) and that for reduction of **Co^{III}** is $\Delta G^\ddagger$(**Co$^{III/II}$**) = $[-0.5 + \lambda_{12}$(**Co$^{III/II}$**)]^2/(4λ_{12}(**Co$^{III/II}$**)) (6−10 kcal mol^{-1}, $-\Delta G^\circ$ for reduction of **Co^{III}** is -0.5 eV). The relative reaction rates for these two ET processes are given by k(**Co$^{II/I}$**)/k(**Co$^{III/II}$**) = exp([$\Delta G^\ddagger$(**Co$^{III/II}$**) $- \Delta G^\ddagger$(**Co$^{II/I}$**)]/RT) = 35 at 295 K.

3. Discussion

TA spectroscopy demonstrates that MV^{2+} oxidatively quenches pulsed-laser excited [Ru(bpy)$_3$]$^{2+}$ to form MV$^{•+}$, which delivers an electron to **Co^{II}**, producing anionic **Co^{I}** and [Ru(bpy)$_3$]$^{3+}$. [Ru(bpy)$_3$]$^{3+}$ oxidizes both **Co^{I}** and **Co^{II}**, and the **Co^{III}**, although formed irreversibly on the electrochemical time scale (possibly owing to changes in ligation),[6] is reduced back to **Co^{II}** by the remaining reductants in solution, **Co^{I}** and MV$^{•+}$. Global analysis supports these assignments, as the TA spectra can be modeled as linear combinations of steady-state absorption spectra of the starting compounds and the transiently formed ET species. Kinetics traces (Figure 3) measured at 730 nm provide information about ET in the system. The rate law for the coupled series of ET reactions (Schemes 1 and S1, Supporting Information) was solved numerically to produce time-dependent concentration profiles for all species which, with molar extinction coefficients and selected independently determined rate constants, allowed us to simulate the observed kinetics and extract elementary rate constants. The specific rate for **Co^{II}** reduction by MV$^{•+}$ is 2.0 × 10^8 M^{-1} s^{-1} and those for **Co^{I}** oxidations by [Ru(bpy)$_3$]$^{3+}$ and **Co^{III}** are 9.8 × 10^9 M^{-1} s^{-1} and 4.4 × 10^8 M^{-1} s^{-1}, respectively. Rate constants for two other ET reactions were extracted from the simulations: **Co^{II}** oxidation by [Ru(bpy)$_3$]$^{3+}$ (5.2 × 10^7 M^{-1} s^{-1}); and **Co^{III}** reduction by MV$^{•+}$ (6.0 × 10^6 M^{-1} s^{-1}).

The specific rates of **Co^{III}**−**Co^{II}** and **Co^{II}**−**Co^{I}** electron self-exchange reactions can be estimated using the Marcus cross relation.[13] Taking the rate constants for reductions of [Ru(bpy)$_3$]$^{3+}$ by **Co^{II}** and **Co^{III}** by MV$^{•+}$, we estimate that the **Co^{III}**−**Co^{II}** rate constant is between 9.5 × 10^{-8} and 2.6 × 10^{-5} M^{-1} s^{-1}. This value is lower than that estimated for [Co$^{III/II}$(dmgBF$_2$)$_2$(H$_2$O)$_2$]$^{+/0}$ in aqueous solution (1.7 × 10^{-4}

(14) Young, R. C.; Keene, F. R.; Meyer, T. J. *J. Am. Chem. Soc.* **1977**, *99*, 2468–2473.

(15) Chan, M.-S.; Wahl, A. C. *J. Phys. Chem.* **1978**, *82*, 2542–2549.

(16) Rieger, A. L.; Rieger, P. H. *J. Phys. Chem.* **1984**, *88*, 5845–5851.

(17) Felton, G. A. N.; Glass, R. S.; Lichtenberger, D. L.; Evans, D. H. *Inorg. Chem.* **2006**, *45*, 9181–9184.

Table 1. Reaction Parameters for Co(dpgBF$_2$)$_2$(CH$_3$CN)$_2$

cross reaction	k_{11} reaction	k_{22} reaction	ΔE (V)[a]	K_{12}	k_{12} (M^{-1} s^{-1})	k_{11} (M^{-1} s^{-1})	k_{22} (calcd) (M^{-1} s^{-1})	λ (eV)
6	Ru(bpy)$_3$$^{3+/2+}$	Co^{III}/Co^{II}	0.97	4.74×10^{16}	5.2×10^7	2.0×10^{9b}	9.5×10^{-8}	4.19
						7.3×10^{6c}	2.6×10^{-5}	3.60
7	MV$^{2+/\cdot+}$	Co^{III}/Co^{II}	0.76	1.16×10^{13}	6.0×10^6	5.4×10^{8d}	9.3×10^{-7}	3.97
						Avg.		3.9 ± 0.3
3	Ru(bpy)$_3$$^{3+/2+}$	MV$^{2+/\cdot+}$	1.73	5.52×10^{29}	5.7×10^9	2.0×10^{9b}	6.2×10^2	1.91
						7.3×10^{6c}	1.7×10^5	1.34
4	MV$^{2+/\cdot+}$	Co^{II}/Co^{I}	0.18	1.24×10^3	2.0×10^8	5.4×10^{8d}	1.2×10^{5e}	1.38^f

[a] See Supporting Information. [b] Reference 14. [c] Reference 15. [d] Reference 16 [e] Estimated uncertainty ± 0.5 M^{-1} s^{-1}. [f] Estimated uncertainty ± 0.05 eV.
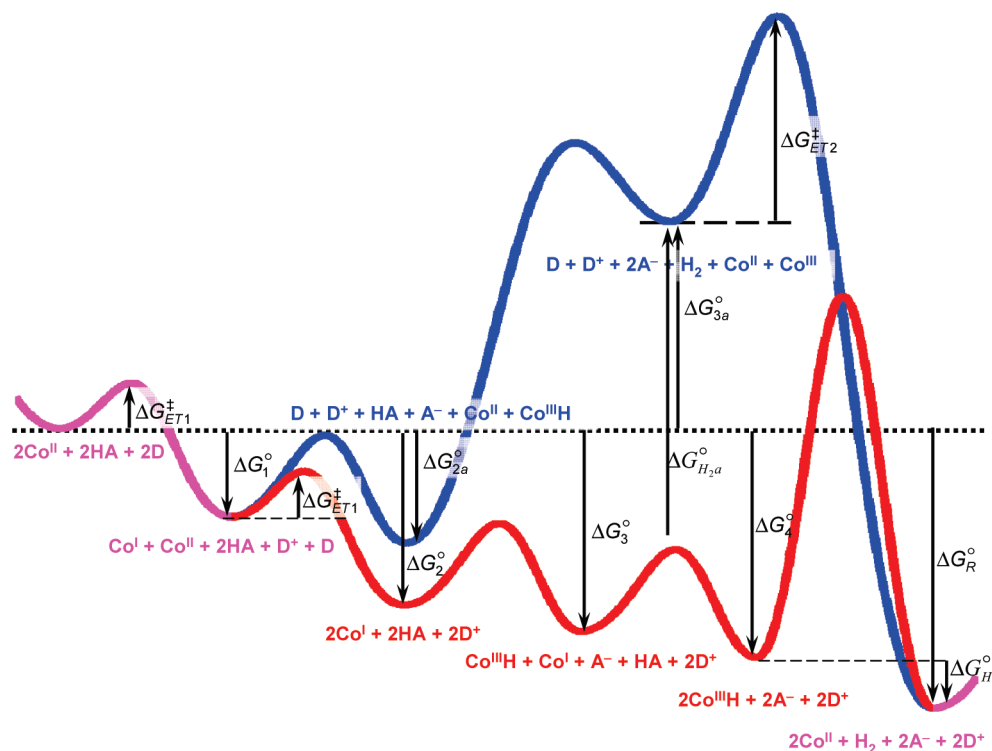

Figure 4. Thermodynamic analysis of the homolytic and heterolytic pathways for hydrogen evolution. D is a reductant. Values for barriers and driving forces are given in Table S3, Supporting Information.

M^{-1} s^{-1} to 8.7×10^{-3} M^{-1} s^{-1}).[18] Corresponding self-exchange rate constants for [Co$^{III/II}$(N$_4$)(H$_2$O)$_2$]$^{3+/2+}$ complexes with equatorial tetra-aza macrocylic ligands (4.5×10^{-5} M^{-1} s^{-1} to 5.0×10^{-2} M^{-1} s^{-1}) correlate with structural changes, particularly variations in axial Co–OH$_2$ bond lengths.[19] The rate constant estimated for **Co^{III}–Co^{II}** is near the low end of the range for low-spin Co$^{III/II}$ complexes in aqueous solution.

Using the rate constants for **Co^{II}** reduction by MV$^{\cdot+}$, we can estimate the **Co^{II}–Co^{I}** self-exchange rate constant to be 1.2 (± 0.5) $\times 10^5$ M^{-1} s^{-1}. While we determined the rate constant for **Co^{I}** oxidation by [Ru(bpy)$_3$]$^{3+}$, the large driving force for this reaction (1.55 eV) places it in the Marcus inverted region where calculation of self-exchange rate constants is unreliable. The stark difference between the **Co^{III}–Co^{II}** and **Co^{II}–Co^{I}** rates is similar to that found for [Co^{II}(bpy)$_3$]$^{2+}$ ([Co$^{III/II}$(bpy)$_3$]$^{3+/2+}$,

18 M^{-1} s^{-1}; [Co$^{II/I}$(bpy)$_3$]$^{2+/+}$, $\sim 10^9$ M^{-1} s^{-1}).[20] The reactivity differences are attributable to the substantial nuclear configuration changes that accompany [Co$^{III/II}$(bpy)$_3$]$^{3+/2+}$ exchange (Δd_0 for Co–N bonds = 0.19 Å), and the modest rearrangements upon [Co^{II}(bpy)$_3$]$^{2+}$ reduction to [Co^{I}(bpy)$_3$]$^+$ ($\Delta d_0 = -0.02$ Å). It is interesting to note that a pronounced change is found in the solid-state structures of **Co^{II}** and **Co^{I}**: an axial CH$_3$CN ligand is lost upon reduction, accompanied by a 0.268 Å shortening of the remaining nitrile bond, 0.27 Å displacement of the **Co^{I}** ion, and a 0.035 Å reduction of the Co–N$_{imine}$ distance.[6] These considerable structural changes are at variance with the large **Co^{II}–Co^{I}** electron self-exchange rate constants extracted using the cross relation. The discrepancy may be an indication that electron transfer and the large structural rearrangements occur in separate elementary reaction steps. The large nuclear rearrangements expected for oxidation of **Co^{II}** to **Co^{III}**, however, are reflected in the **Co^{III}–Co^{II}** self-exchange rate constant.[18]

(18) Wangila, G. W.; Jordan, R. B. *Inorg. Chim. Acta* **2005**, *358*, 2804–2812.

(19) Endicott, J. F.; Durham, B.; Glick, M. D.; Anderson, T. J.; Kuszaj, J. M.; Schmonsees, W. G.; Balakrishnan, K. P. *J. Am. Chem. Soc.* **1981**, *103*, 1431–1440.

(20) Szalda, D. J.; Creutz, C.; Mahajan, D.; Sutin, N. *Inorg. Chem.* **1983**, *22*, 2372–2379.

The reorganization parameter, λ, which accounts for both inner- and outer-sphere rearrangements accompanying an ET process, can be estimated from self-exchange rates. The reorganization energy for $\mathbf{Co^{III}}$–$\mathbf{Co^{II}}$ self-exchange is 3.9 (± 0.3) eV (89.9 (± 6.9) kcal mol^{-1}), while that for the $\mathbf{Co^{II}}$–$\mathbf{Co^{I}}$ reaction is substantially smaller, about 1.4 (± 0.05) eV (34.6 (± 1.2) kcal mol^{-1}). These calculations emphasize the formidable energy barriers associated with a hydrogen-evolving mechanism that requires a $\mathbf{Co^{III}}$ intermediate.

The large reorganization energy associated with $\mathbf{Co^{III}}$–$\mathbf{Co^{II}}$ electron transfer implies that the barrier to reduction of $\mathbf{Co^{III}}$ by D ($\Delta G_{ET2}^{\ddagger}$) is about 2.1 kcal mol^{-1} higher than that of $\mathbf{Co^{II}}$ ($\Delta G_{ET1}^{\ddagger}$), corresponding to a $\sim$35-fold lower specific rate. The largest barriers to catalysis, then, likely will be associated with the elementary steps that form H_2.[21] Protonation of $\mathbf{Co^{III}H}$ leads to release of H_2 and generation of $\mathbf{Co^{III}}$ in the heterolytic pathway, and the driving force for this reaction ($-\Delta G_{H_{2a}}^{o}$, which depends on $E^{o}(\mathbf{Co^{III/II}})$ (relative to $E^{o}(HA/H_2)$ is in most cases thermodynamically unfavorable. Thus, the barrier for this elementary step ($\Delta G_{H_{2a}}^{\ddagger}$) is estimated to be greater than 11 kcal mol^{-1}, the lower limit for $\Delta G_{H_{2a}}^{o}$. Little is known about the rate of bimolecular reductive elimination of H_2 from metal hydrides (homolytic path). Under the assumption of rapid electron and proton transfers such that $\mathbf{Co^{II}}$, $\mathbf{Co^{I}}$, and $\mathbf{Co^{III}H}$ will be present at their equilibrium concentrations, the rate of H_2 formation (d[H_2]/dt) will be proportional to $k_{H_2}[\mathbf{Co^{III}H}]^2$ for the homolytic pathway and to $k_{H_{2a}}[HA][\mathbf{Co^{III}H}]$ for the heterolytic route. Ultimately, the dominance of one path over the other during catalysis depends not just on the relative barrier heights for H_2 elimination but also on the relative concentrations of HA and $\mathbf{Co^{III}H}$.[22]

4. Conclusions

Thermodynamic analysis of two proton reduction pathways reveals that the driving force for H_2 production in the homolytic pathway depends on $E^{o}(\mathbf{Co^{II/I}})$ (relative to $E^{o}(HA/H_2)$) and the difference in pK_a between $\mathbf{Co^{III}H}$ and HA. In the heterolytic pathway, $E^{o}(\mathbf{Co^{III/II}})$ is an additional determinant that, in most cases, renders heterolytic H_2 evolution extremely unfavorable.[23] Furthermore, the barrier associated with reduction of transiently generated $\mathbf{Co^{III}}$ is significantly higher than that for $\mathbf{Co^{II}}$. Although the heterolytic route can dominate at very high acid concentrations, the relatively high energy barriers and unfavorable driving forces are significant. While little is known about the barrier to the $\mathbf{Co^{III}H}$ bimolecular reaction, covalently linking two $\mathbf{Co^{III}H}$ complexes could substantially increase the rate of H_2 production by decreasing the volume required for diffusional collisions.

5. Experimental Section

5.1. Reagents. Syntheses of air- and moisture-sensitive compounds were carried out using Schlenk techniques or in a nitrogen atmosphere glovebox. Solvents for these syntheses were dried by a standard method[24] or over activated sieves followed by passage over activated alumina. CD$_3$CN was obtained from Cambridge Isotope Laboratories, Inc. All materials, unless noted, were used

as received. Elemental analysis was performed by Columbia Analytical Services, Tuscon, AZ.

All samples were prepared in high purity (>99.99%) CH$_3$CN (EMD) in a high-vacuum 1-cm path length fused quartz cell (Starna Cells) connected to a 10 mL bulb. A typical sample was prepared as follows. In an inert atmosphere glovebox, a 2 mL solution of $\sim$126–314 μM Co(dpgBF$_2$)$_2$(MeCN)$_2$ and a 2 mL solution of $\sim$40 μM [Ru(bpy)$_3$][PF$_6$]$_2$, 7 mM [MV][PF$_6$]$_2$, and 0.2 M NBu$_4$PF$_6$ in dry, degassed CH$_3$CN were placed into the cell and isolated from atmosphere and the bulb by a high-vacuum Teflon valve (Kontes).

Co(dpgBF$_2$)$_2$(CH$_3$CN)$_2$ was synthesized under an inert atmosphere with degassed solvents according to a literature method,[25] recrystallized in CH$_3$CN, and analyzed by cyclic voltammetry, absorption measurements, and elemental analysis. The hexafluorophosphate salts of [Ru(bpy)$_3$]$^{2+}$ and methyl viologen ([MV]$^{2+}$) were prepared from the corresponding chloride salts via salt metathesis with NH$_4$PF$_6$ in water (0 °C).

Na[Co(dpgBF$_2$)$_2$(CH$_3$CN)] was prepared by reaction of Co(dpgBF$_2$)$_2$(CH$_3$CN)$_2$ with excess sodium mercury amalgam (0.5% Na) under vacuum in anhydrous acetonitrile, analogous to a literature preparation.[6] The reduced species was transferred over a frit to a fused 2-mm quartz cuvette; the reduction process was monitored via UV–vis absorption spectroscopy until the reduction was complete.

Methyl viologen cation radical (MV$^{\bullet+}$) was prepared *in situ* by the photolysis (Hg lamp) of a degassed sample containing 10 μM [Ru(bpy)$_3$][PF$_6$]$_2$, 84 μM [MV][PF$_6$]$_2$, 0.1 M NBu$_4$PF$_6$, and 0.1 M triethanolamine in CH$_3$CN for 2 h. The resulting absorption spectrum matched the literature spectrum.[26]

[Ru(bpy)$_3$]$^{3+}$ was prepared *in situ* by oxidizing [Ru(bpy)$_3$]$^{2+}$ with ammonium cerium nitrate (Ce^{IV}) according to a literature method.[27]

MeCo(dpgBF$_2$)$_2$(L) (L = H$_2$O, CH$_3$CN) was prepared by a method similar to that of Ram et al.[28] for MeCo(dmgBF$_2$)$_2$(H$_2$O). Co(dpgBF$_2$)$_2$(CH$_3$CN)$_2$ (0.505 g, 0.724 mmol) was suspended under argon in 22 mL of degassed CH$_3$OH in a two-neck 100 mL round-bottom flask equipped with a septum, vacuum adaptor, and stirbar. NaOH (0.091 g, 2.3 mmol) was added, and the solution was stirred until the NaOH dissolved, followed by addition of pyridine (0.058 g, 0.733 mmol). After cooling the suspension to 0 °C, NaBH$_4$ (0.046 g, 1.21 mmol) was added, the reaction was stirred 15 min, and the suspension turned a blue-gray color. Methyl trifluoromethanesulfonate (1 g, 6.1 mmol) was added via syringe, and the suspension turned yellow-brown over 10 min. The reaction was then exposed to the atmosphere, at which time 1 mL of pyridine and 40 mL of H$_2$O were added 5 min apart. After 10 min of stirring, the product was filtered to yield a yellow-brown solid, and this was washed with 3 × 40 mL of H$_2$O. Then the product was collected, placed in a round-bottom flask, suspended in 30 mL of 6 M HClO$_4$ and stirred for 20 min to remove pyridine. The suspension was then filtered to yield a yellow-brown solid and washed with 2 × 30 mL of HClO$_4$ followed by copious amounts of H$_2$O and 30 mL of hexanes. The yellow-brown solid was collected (315 mg, 65%). Vapor diffusion of ether into a saturated CH$_3$CN solution of MeCo(dmgBF$_2$)$_2$(CH$_3$CN) afforded a yellow powder. ^{1}H NMR (300 MHz, CD$_3$CN): δ 7.28–7.48 (m, 20H, Ph), δ 1.87 (s, 3H, CH$_3$) ppm. HRMS (FAB+), m/z calculated for C$_{31}$H$_{26}$B$_2$F$_4$N$_5$O$_4$Co (L = CH$_3$CN): 689.14. Found: 690.1559 (M + H), 628.7951 (M − C$_6$H$_5$), 565.7864 (M − C$_6$H$_5$ − BF$_2$ + H), 513.9995 (M − C$_6$H$_5$ − 2 BF$_2$), 485.9959 (M − M − C$_6$H$_5$ − 2 BF$_2$ − 2 CH$_3$). Elemental analysis calculated for C$_{29}$H$_{25}$B$_2$F$_4$N$_4$O$_5$Co (L = H$_2$O): C, 52.29; H, 3.78; N, 8.41. Found: C, 52.62; H, 3.95; N, 8.31.

(21) Bhugun, I.; Lexa, D.; Savéant, J.-M. *J. Am. Chem. Soc.* **1996**, *118*, 3982–3983.
(22) Chao, T.-H.; Espenson, J. H. *J. Am. Chem. Soc.* **1978**, *100*, 129–133.
(23) Kellett, R. M.; Spiro, T. G. *Inorg. Chem.* **1985**, *24*, 2373–2377.
(24) Pangborn, A. B.; Giardello, M. A.; Grubbs, R. H.; Rosen, R. K.; Timmers, F. J. *Organometallics* **1996**, *15*, 1518–1520.

(25) Tovrog, B. S.; Kitko, D. J.; Drago, R. S. *J. Am. Chem. Soc.* **1976**, *98*, 5144–5153.
(26) Kosower, E. M.; Cotter, J. L. *J. Am. Chem. Soc.* **1964**, *86*, 5524–5527.
(27) Bryant, G. M.; Fergusson, J. E. *Aust. J. Chem.* **1971**, *24*, 275–286.
(28) Ram, M. S.; Riordan, C. G.; Yap, G. P. A.; Liable-Sands, L.; Rheingold, A. L.; Marchaj, A.; Norton, J. R. *J. Am. Chem. Soc.* **1997**, *119*, 1648–1655.

5.2. Physical Methods. NMR spectra were recorded using a Varian Mercury 300 spectrometer. ^{1}H NMR chemical shifts were referenced to residual solvents as determined relative to Me$_4$Si (δ = 0 ppm). High resolution mass spectra (HRMS) were obtained at the California Institute of Technology Mass Spectrometry Facility. UV−visible absorption measurements were carried out using a Hewlett-Packard 8452 spectrophotometer in 0.2 or 1 cm path length quartz cuvettes.

Time-resolved spectroscopic measurements were carried out at the Beckman Institute Laser Resource Center. Laser excitation was provided by 8-ns pulses from a 10 Hz Q-switched Nd:YAG laser (Spectra-Physics Quanta-Ray PRO-Series). The third harmonic was either used directly or to pump an optical parametric oscillator (OPO, Spectra-Physics Quanta-Ray MOPO-700, tunable in the visible region).

Probe light for transient absorption kinetics measurements was provided by a 75-W arc lamp (PTI model A 1010) that could be operated in continuous wave or pulsed modes. Timing between the laser and the probe light was controlled by a digital delay generator (EG&G 9650). Sample excitation (λ = 480 nm) by the laser beam was collinear with the probe light; scattered excitation light was rejected by suitable long pass and short pass filters, and probe wavelengths were selected for detection by a double monochromator (Instruments SA DH-10) with 1 mm slits. Transmitted light was detected with a photomultiplier tube (PMT, Hamamatsu R928). The PMT current was amplified and recorded with a transient digitizer (LeCroy 9354A or Tektronix DSA 602). Absorption data were averaged over at least 500 laser pulses. The data were converted to units of ΔOD ($\Delta OD = -\log_{10}(I/I_0)$, where I is the time-resolved probe-light intensity with laser excitation, and I_0 is the intensity without excitation). Samples measured on the microsecond time scale or faster were stirred and measured using a laser repetition rate of 10 Hz, while samples measured on a millisecond time scale were excited with a single shutter-released laser pulse, stirred for 1 s after collecting data, then allowed to sit until the solution settled (2 s) before the next laser pulse. Data were averaged over approximately 500 shots.

Probe light for transient absorption spectra was provided by white light flash lamp sources with either nanosecond or microsecond durations. Probe light was transported via a fiber optic and split by a partial reflector. Approximately 70% of the probe light was passed through the sample, with the remainder directed around the sample as a reference beam. Sample excitation (λ_{ex} = 355 nm) by the laser beam was collinear with the probe light. Light intensity was read by two photodiode arrays (Ocean Optics S1024DW Deep Well Spectrometer), with scattered excitation light rejected by a 370 nm long pass filter. The timing synchronization of the laser fire, flashlamp fire, and photodiode array readout were controlled by a series of timing circuits triggered by either a Q-switch advance logic pulse for nanosecond (or a laser lamp sync pulse for microsecond) lamp measurements. The photodiode readout was interfaced with a PC via a National Instruments multifunction input/output card. Measurements were made with and without excitation, corrected for background light, and corrected for fluorescence when necessary. Difference spectra were averaged over approximately 500 shots.

All instruments and electronics in these systems were controlled by software written in LabVIEW (National Instruments). Data manipulation was performed with MATLAB R2008a (Mathworks, Inc.) and graphed with Igor Pro 5.01 (Wavemetrics).

5.3. Data Analysis. Global analysis and kinetics simulations were performed in MATLAB, the latter using the ordinary differential equation solver ode23s (Rosenbrock method) and an m-file with the differential equations. [Ru(bpy)$_3$]$^{2+*}$ luminesces weakly at the wavelength the kinetics traces were measured. Because of the finite amplifier response for the longer time scales, the first few microseconds of data were obscured by this emission process.

Supporting Information Available: Full details of absorption measurements, global analysis, kinetics modeling, reduction potentials, and thermodynamic analysis. This information is available free of charge via the Internet at http://pubs.acs.org.

JA9080259